NASA-TM-111605

AIAA 96-2544
High Reynolds Number Analysis of Flat Plate and Separated Afterbody Flow Using Non-Linear Turbulence Models

John R. Carlson
NASA Langley Research Center
Hampton, VA

32nd AIAA/ASME/SAE/ASEE Joint Propulsion Conference & Exhibit

July 1–3, 1996 / Lake Buena Vista, Florida

HIGH REYNOLDS NUMBER ANALYSIS OF FLAT PLATE AND SEPARATED AFTERBODY FLOW USING NON-LINEAR TURBULENCE MODELS

John R. Carlson*
NASA Langley Research Center
Hampton, VA

Abstract

The ability of the three-dimensional Navier-Stokes method, PAB3D, to simulate the effect of Reynolds number variation using non-linear explicit algebraic Reynolds stress turbulence modeling was assessed. Subsonic flat plate boundary-layer flow parameters such as normalized velocity distributions, local and average skin friction, and shape factor were compared with DNS calculations and classical theory at various local Reynolds numbers up to 180 million. Additionally, surface pressure coefficient distributions and integrated drag predictions on an axisymmetric nozzle afterbody were compared with experimental data from 10 to 130 million Reynolds number. The high Reynolds data was obtained from the NASA Langley 0.3m Transonic Cryogenic Tunnel. There was generally good agreement of surface static pressure coefficients between the CFD and measurement. The change in pressure coefficient distributions with varying Reynolds number was similar to the experimental data trends, though slightly over-predicting the effect. The computational sensitivity of viscous modeling and turbulence modeling are shown. Integrated afterbody pressure drag was typically slightly lower than the experimental data. The change in afterbody pressure drag with Reynolds number was small both experimentally and computationally, even though the shape of the distribution was somewhat modified with Reynolds number.

Introduction

Current focused program efforts are considering Reynolds number scaling a significant aspect of aircraft testing and development. Wing aerodynamics and flow about propulsion systems can have considerable sensitivity to varying Reynolds number. Most of the sub-scale wind tunnel testing occurs at Reynolds numbers below that of flight conditions; therefore, the ability of computational fluid dynamics (CFD) to simulate higher Reynolds number flow is of importance.

Previous to the development of cryogenic test techniques for achieving high Reynolds numbers in wind tunnel facilities, little fundamental research data had been available for the evaluation of any theoretical methods to predict these effects. Several years ago, during the development phase of cryogenic testing techniques at the NASA Langley Research Center; two sets of simple axisymmetric nacelle models were built and tested in what was then known as the 1/3m Pilot Transonic Cryogenic Tunnel (now the 0.3m Transonic Cryogenic Tunnel). This was some of the first set of test data for nozzle-boattail geometries taken over a large range of Reynolds numbers, refs. 1–4.

The current investigation assesses the capability of the Navier-Stokes method PAB3D, version 13S, (refs. 5–8) using non-linear algebraic Reynolds stress turbulence models to predict the Reynolds number effects on the flow about a nozzle boattail, and simulate a 5 meter flat plate at very high Reynolds numbers. Comparisons were made with wind tunnel data for the boattail geometry and boundary layer profiles, shape factor, and skin friction with DNS data and textbook equations for incompressible flat plate flow.

Nomenclature

A_{max}	maximum body cross-sectional area, 0.78539 in^2
C_D	pressure drag coefficient, $\frac{F}{q_\infty A_{max}}$
C_F	average skin friction coefficient, $\frac{1}{l q_\infty} \sum \tau_w \Delta l$
C_f	local skin friction coefficient, τ_w / q_∞
C_p	pressure coefficient, $\frac{p - p_\infty}{q_\infty}$
d_m	body maximum diameter, 1.0 in.
F	axial force along body axis
f_μ	near-wall damping function for linear $K-\varepsilon$
GS	Gatski-Speziale
H_{12}	boundary layer shape factor, δ_1/δ_2
H_{32}	boundary layer shape factor, δ_3/δ_2
h_1	physical height of first computational grid from a wall
K	turbulent kinetic energy
l	integration length of flat plate
L	model reference length
M	Mach number
N_{Re}	Reynolds number based on model reference length
n	direction normal to wall
$\overline{P}$	production term for turbulent kinetic energy
p	static pressure, Pa
q	dynamic pressure, Pa
R_L	Reynolds number based on flat plate integration length
R_T	cell turbulent Reynolds number, $K^2/\nu\epsilon$
R_x	Reynolds number based on distance x, $u_\infty x/\nu$

*Senior Scientist, Component Integration Branch, Aerodynamics Division. Senior Member AIAA.

R_{δ_1}	displacement thickness Reynolds number, $u_\infty \delta_1 / \nu$
R_θ	momentum thickness Reynolds number, $u_\infty \delta_2 / \nu$
t	time
S	strain tensor
SZL	Shih, Zhu & Lumley
$\overline{U}$	magnitude of local velocity, $\sqrt{\sum {u_k}^2}$
u	stream-wise velocity
u_k	cartesian velocity components
u^+	law-of-the-wall coordinate, u/u_τ
u_τ	friction velocity, $\sqrt{(\tau_w/\rho)}$
$u'v'^+$	nondimensional shear stress, $u'v'/{u_\tau}^2$
W	vorticity tensor
x	stream-wise distance
y^+	law-of-the-wall coordinate, nu_τ/ν
z	vertical distance
Δl	incremental distance on flat plate
δ_1	boundary layer displacement thickness
δ_2	boundary layer momentum thickness
δ_3	boundary layer energy thickness
ϵ	turbulent dissipation
μ	laminar viscosity
μ_t	turbulent viscosity
μ_w	local laminar viscosity at the wall
ν	kinematic viscosity, μ/ρ
ρ	density
τ	shear stress
ϕ	angular location of pressure orifices, *deg*

Superscripts

L	laminar
T	turbulent

Subcripts

β	nozzle boattail component contribution
CL	centerline
fp	flat plate
l	laminar
n	non-linear component
t	turbulent
$t0$	free stream total condition
sf	skin friction contribution
$w, wall$	condition at the wall surface
∞	free stream condition

Computational Procedure

Governing Equations

The code used was the general three dimensional (3-D) Navier-Stokes method PAB3D, version 13S. This code has several computational schemes, different turbulence models, and viscous stress models that can be utilized, as described in more detail in refs. 5 through 8. The governing equations are the Reynolds-averaged simplified Navier-Stokes equations (RANS) obtained by neglecting all stream-wise derivatives of the viscous terms. The resulting equations are written in generalized coordinates and conservative form. Viscous model options include k-thin layer, j-thin layer, jk-uncoupled and jk-coupled simulations. Typically the thin-layer viscous assumption of the full 3-D viscous stresses is utilized. Experiments such as the investigation of supersonic flow in a square duct was found to require fully coupled 2 directional viscosity to properly resolve the physics of the secondary cross-flow. The Roe upwind scheme with first, second, or third order accuracy can be used in evaluating the explicit part of the governing equations and the van Leer scheme is used to construct the implicit operator. The diffusion terms are centrally differenced and the inviscid flux terms are upwind differenced. Two finite volume flux-splitting schemes are used to construct the convective flux terms.

All solutions were developed using third-order accurate schemes for the convective terms, and second-order for the viscous diffusion terms, denoted by the first 3 in the nomenclature in the figures and tables and the min-mod solution limiter, denoted by the second 2 in the nomenclature. Only the viscous model is varied in this study, denoted by the third number in the nomenclature. For completeness, a table of nomenclature designating the order of scheme, limiter, and viscous modeling is given below. Other solution limiters include van Albeda, Spekreijse-Venkat (S-V) and a modified S-V (ref. 9). Solution limiters influence solution convergence and final results. In some instances, such as a jet-plume simulation, the van Albeda solution limiter is required to obtain a smooth converged solution.

Nomenclature	Solution Limiter	Viscous model
311	van Albeda	k-thin layer
312	van Albeda	jk-coupled
313	van Albeda	jk-uncoupled
321	min-mod	k-thin layer
322	min-mod	jk-coupled
323	min-mod	jk-uncoupled
331	S-V	k-thin layer
332	S-V	jk-coupled
333	S-V	jk-uncoupled
341	modified S-V	k-thin layer
342	modified S-V	jk-coupled
343	modified S-V	jk-uncoupled

The code can utilize either a 2-factor or 3-factor numerical scheme to solve the flow equations. The 2-factor scheme is typically used as it requires 10 to 15 percent less memory as compared to the 3-factor scheme. The memory difference is dependent on the size of cross-planes of the specific grid being used. When the 2-factor scheme is used the orientation of the grid and predominate flow direction typically along the i grid index, such that the Roe scheme is utilized to sweep stream-wise through the computational domain and the van Leer scheme for the solution of the cross-plane

(i.e., i = constant) of a 3-D problem. However solving a single-cell wide two-dimensional (2-D) mesh defined with the i direction of the grid oriented in the conventional stream-wise direction will typically converge slower using the Roe relaxation solution scheme compared to solving the equivalent problem with the van Leer scheme. Therefore the i and j directions of a 2-D mesh are swapped allowing the entire flow-field to be solved implicitly with each iteration. The explicit sweep is not used since only one cell exists in the i direction. The implicit scheme usually has a much higher rate of convergence and typically provides a solution using less computational time.

Turbulence Simulation

The turbulence model equations are uncoupled from the RANS equations and are solved with a different time step, typically 1/2, than that of the principle flow solution. A considerably lower principle Courant-Friedrichs-Levy (CFL) number is typically required to solve problems if both the main flow equations and turbulence equations are solved iteratively using identical time rates. Larger time step differences, e.g., 1/4 to 1/8, slow solution convergence further but result in identical final solutions. Flow solution transients at times require the turbulence equations time step to be reducted temporarily. Turbulence simulations are resolved at all grid levels, not just at the finest grid level.

Version 13S of the PAB3D code used in this study has options for several algebraic Reynolds stress (ASM) turbulence simulations. The Standard model coefficients of the $K-\varepsilon$ equations were used as the basis for all the linear and non-linear turbulent simulations, ref. 10. Additionally, it is known that the eddy viscosity models produce inaccurate normal Reynolds stresses. Flat plate flow, as well as other more complex aerodynamic flows, are anisotropic.

Successful implementation of the algebraic Reynolds stress models required the solution methodology for turbulent production term $\overline{P}$ of the underlying linear turbulence calculations to be modified. $\overline{P}$ depends on high order derivatives of the turbulent Reynolds stresses. Proper representation of the stresses should be provided by face centered values, rather than the cell centered values. Previous attempts to implement non-linear turbulence models in the context of a cell centered eddy viscosity model worked only for 2-D problems and was unable to resolve 3-D flows.

Linear $K-\varepsilon$ equations The transport equation for the turbulent kinetic-energy, K, and the dissipation rate are written as:

$$\frac{\partial \varepsilon}{\partial t}+\overline{u}_k\frac{\partial \varepsilon}{\partial x_k}=\frac{\partial}{\partial x_k}\left((\nu^L+C_\mu\frac{K^2}{\varepsilon})\frac{\partial \varepsilon}{\partial x_k}\right) + C_{\varepsilon 1}\frac{\varepsilon \overline{P}}{K}-C_{\varepsilon 2}\frac{\varepsilon}{K}\left[\varepsilon-2\nu\left(\frac{\partial\sqrt{K}}{\partial n}\right)^2\right] \quad (1)$$

The convective terms are solved using third-order differencing. The diffusion terms are solved using second-order central differencing.

$$\frac{\partial K}{\partial t}+u_k\frac{\partial K}{\partial x_k}=\overline{P}-\varepsilon+\frac{\partial}{\partial x_k}\left[(\nu^L+C_\mu\frac{K^2}{\varepsilon})\frac{\partial K}{\partial x_k}\right] \quad (2)$$

where $\overline{P}=\tau_{ik}^T\frac{\partial u_i}{\partial x_k}$ and ($C_{\varepsilon 1}$=1.44, $C_{\varepsilon 2}$=1.92, C_μ=0.090).

The damping function of Launder & Sharma, ref. 11, $f_\mu=exp\left(-3.41/(1+R_T/50.)^2\right)$, determined the behavior of ε near the wall as a function of turbulent Reynolds number $R_T=K^2/\nu\varepsilon$. The boundary conditions for ε and K at the wall are $\varepsilon_{wall}=2\nu\left(\frac{\partial}{\partial n}\sqrt{K}\right)^2$ and $K_{wall}=0$. The stress components in linear turbulence models are developed with laminar and turbulent components, $\tau_{ij}=\tau_{ij}^L+\tau_{ij}^T$. A generalization of Boussinesq's hypothesis redefines laminar and turbulent components are as follows:

$$\tau_{ij}^L=A^L\delta_{ij}-2\mu^L S_{ij} \quad (3)$$

where

$$A^L=\frac{2}{3}\mu^L S_{kk} \qquad \text{and} \qquad S_{ij}=\frac{1}{2}\left(\frac{\partial u_i}{\partial x_j}+\frac{\partial u_j}{\partial x_i}\right) \quad (4)$$

The turbulent component of the stresses τ_{ij}^T is represented by the sum of linear (T_l) and non-linear (T_n) components. The linear stress is $\tau_{ij}^{T_l}=A^T\delta_{ij}-2\mu^T S_{ij}$ where $A^T=\frac{2}{3}(\rho K+\mu^T S_{kk})$. The non-linear component of the turbulent stresses are addressed in the following section.

Non-Linear Turbulent Stress Equations-- Three theories of explicit algebraic Reynolds stress models were implemented. The Reynold's stress contribution $\tau_{ij}^{T_n}$ used by Shih, Zhu, & Lumley (SZL), (ref. 12) is:

$$\tau_{ij}^{T_n}=2\beta\frac{K^3}{\epsilon^2}\left(W_{ik}\overline{S}_{kj}-\overline{S}_{ik}W_{kj}\right) \quad (5)$$

Gatski & Speziale (GS), (ref. 13);

$$\tau_{ij}^{T_n}=C_\mu^*\frac{K^3}{\varepsilon^2}\left[\beta_1(W_{ik}S_{kj}-S_{ik}W_{kj})+\beta_2(S_{ik}S_{kj}-\frac{1}{3}S_{mn}S_{mn}\delta_{ij})\right] \quad (6)$$

and Girimaji (G), (ref. 14);

$$\tau_{ij}^{T_n}=2C_\mu^*\frac{K^3}{\varepsilon^2}\left[-G_2\left(W_{ik}S_{kj}-S_{ik}W_{kj}\right)+G_3(S_{ik}S_{kj}-\frac{1}{3}S_{mn}S_{mn}\delta_{ij})\right] \quad (7)$$

where

$$W_{ij}=\frac{1}{2}\left(\frac{\partial u_i}{\partial x_j}-\frac{\partial u_j}{\partial x_i}\right)$$

$$\overline{S}_{ij}=S_{ij}-\frac{1}{3}S_{kk}\delta_{ij}$$

The turbulent viscosity, μ^T, is defined as

$$\mu^T=C_\mu^*\left(\frac{\rho K^2}{\epsilon}\right) \quad (8)$$

where $C_\mu^* = f_\mu C_\mu$ for solutions solving linear turbulence simulations and equal to the variable function $C_\mu^* = f(S, W, K, \epsilon)$ for solutions involving algebraic Reynolds stress simulations. Functions for C_μ^* take the following forms for each of the ASM.

Shih, Zhu & Lumley, (ref. 12):

$$C_\mu^* = 1/\left(6.5 + A_s^* \frac{U^* K}{\epsilon}\right) \tag{9}$$

Gatski-Speziale, (ref. 13):

$$C_\mu^* = const. * (1+\chi^2)/(3+\chi^2+6\chi^2\psi^2+6\psi^2) \tag{10}$$

A_s^*, U^*, χ, and ψ are all different functions of the strain and vorticity tensors and are detailed in the references.

Girimaji, (ref. 14):

$$G_1 = \begin{cases} L_0^1 L_2 / \left[(L_1^0)^2 + 2\eta_2 (L_4)^2\right] & \text{for } \eta_1 = 0; \\ L_0^1 L_2 / \left[(L_1^0)^2 + \frac{2}{3}\eta_1 (L_3)^2 + 2\eta_2 (L_4)^2\right] & \text{for } L_1^1 = 0; \\ -\frac{p}{3} + \left(-\frac{b}{2} + \sqrt{D}\right)^{\frac{1}{3}} + \left(-\frac{b}{2} - \sqrt{D}\right)^{\frac{1}{3}} & \text{for } D > 0; \\ -\frac{p}{3} + 2\sqrt{\frac{-a}{3}}\, cos(\frac{\theta}{3}) & \text{for } D < 0 \text{ and } b < 0; \\ -\frac{p}{3} + 2\sqrt{\frac{-a}{3}}\, cos(\frac{\theta}{3} + \frac{2\pi}{3}) & \text{for } D < 0 \text{ and } b > 0. \end{cases} \tag{11}$$

The variable G_1 utilized by Girimaji is equal to $-C_\mu^*$. A compilation of the parameters used in Girimaji's model can be found in the Appendix. Additional information is in reference 14.

The solution processes for wall-bounded flows were equally robust for each of the models. Previous results, not published here, show Gatski-Speziale requiring lower CFL numbers for the solution of free-shear flows. Obtaining converged solutions using Gatski's C_μ^* were found to be problem dependent. Girimaji's G_1 function appears to be extremely well behaved permitting for fairly high CFL numbers to used.

Turbulent Trip Equations– The technique used for initializing the viscous flow transition from laminar to turbulent is placing K and ϵ profiles at user-specified lines or planes in the flowfield. The line or plane of the specified trip area is surveyed for the maximum and minimum velocity and vorticity along that line and a shape function from 0 to 1 is created of the form $F = (f - f_{min})/(f_{max} - f_{min})$ where f is a product of the velocity and vorticity $f = u|W|, |W| = 2\sqrt{\sum W_{ij}^2}$. The turbulent kinetic energy profile is then $K = \alpha\ \overline{U}\ F$, where α is a free parameter determining the magnitude of the impulse as a percent of local total velocity, $\overline{U}$. The typical value specified by the user, and used for this paper, is 2% (or $\alpha = 0.02$). The ϵ profile is developed from the assumption that production $\overline{P}$ is equal to the dissipation ϵ equaling $C_\mu \frac{K^2}{\epsilon} 2\mu \overline{S}_{ij} \frac{\partial u_i}{\partial x_j}$. The result of the initialization is seen as a spike in the K field of the solution. This initial turbulent profile develops as permitted by the local flow conditions.

Solution Process

Turbulent flow solutions using ASM and two-equation linear $K - \epsilon$ model requires 23 words per grid point. The code speed is dependent on the turbulence model, thin-layer assumptions and numerical schemes. The following table are some options available in the code with C-90 timing in μseconds/iteration/grid point.

Solver Scheme	Viscous Modeling	Turbulence Modeling (3^{rd}-order)	Stress Center	Timing C-90 μs/iter/grid
2-factor	j-k uncoupled	Girimaji ASM	Face	23
2-factor	k thin-layer	Girimaji ASM	Face	20
Diagonalization	j-k uncoupled	Girimaji ASM	Face	16
Diagonalization	k thin-layer	Girimaji ASM	Face	14
2-factor	k thin-layer	Gatski & Speziale ASM	Face	19
2-factor	k thin-layer	SZL ASM	Face	20
2-factor	k thin-layer	Linear-Isotropic	Face	18
2-factor	k thin-layer	Linear-Isotropic	Cell	17
Diagonalization	k thin-layer	Linear-Isotropic	Face	12

Several parameters were used to gauge solution convergence. Local skin friction, shape factor and solution residual were monitored for convergence of the flat plate solutions. Total afterbody drag, nozzle pressure drag, and solution residual were used to determine the solution status at the coarse (144), medium (122), and fine (111) grid levels of the axisymmetric afterbody. The 144 abbreviation means divide number of i-cells by 1, number of j-cells by 4 and the number of k-cells by 4. Afterbody drag variance of less than 0.50 percent for several hundred iterations was achieved for all test cases.

The conservative patch interface package of Pao and Abdol-Hamid (ref. 7) enables the code to properly transmit information between mis-matched block interfaces. Integer-to-one interfaces are considered a subset of the arbitrary block interface and do not need to be specified as such to the patching code. The patching program is a preprocessor that writes a connectivity data base prior to the start of the first solution. Each entry to the patch data base contains cell face areas and indices relating that cell with all other cells that will share momentum flux information. The data base information is automatically re-allocated internal to the code during mesh sequencing. As a result, each block can be sequenced at different levels and the correct interface information is maintained at the cell level. However, it is important to note that features in the flow developed on one side of an interface should not be obliterated on the other side due to an excessive grid density mis-match.

Third-order continuity in transmitting the fluxes across block boundaries is maintained by the code; lower order continuity may be specified by the user if required. As with most Navier-Stokes methods of the type, equal cell size spacing on either side of an interface in directions normal to the interface should be maintained regardless of the mesh sequencing level of the block.

Boundary Conditions

For this study, solid walls were treated as no-slip adiabatic surfaces. The solid wall boundary condition was satisfied by setting the momentum flux of the solid wall cell face

to zero. A boundary condition for the Riemann invariants along the characteristics was specified for the free-stream inflow face and the lateral free-stream outer boundary of the flow domain. An extrapolation boundary condition was applied on the downstream outflow face. The axisymmetric flow assumption for the single-cell grids was implemented by placing flow symmetry conditions to the lateral side boundaries of the computational domain.

Results and Discussion

Subsonic Flat Plate

Flat Plate Grid– The 5 m flat plate multiblock grid had an H-type mesh topology, with the blocking sketched in figure 1. The computational domain included inflow block extending 1 meter upstream from the leading edge of the 5 m flat plate. The initial stream-wise grid spacing at the leading edge of the plate was $1.\times10^{4}$m and was exponentially stretched from the leading edge to the trailing edge at a rate of 5% with a total of 161 grid points. The first cell height was 1.0×10^{6} m fixed at both ends of the plate and exponentially stretched from the surface to the outer boundary at a rate of 11% with a total of 121 grid points. The upper boundary was 2 m away and the lateral width of the grid of 0.01 m. All three blocks had dimensions of 81×121. Tripping to turbulent flow simulation occurred around $R_x = .3$ million or $R_{\delta 1} = 900$, corresponding to a physical distance of approximately 9 mm downstream of the plate leading edge. This allowed for laminar flow to occur over roughly 32 computational cells before tripping to turbulent flow. Grid cell counts were divisible by four to allow a minimum of 2 levels of grid sequencing.

Boundary Layer Characteristics—Figure 2 shows the Reynolds number based on length variation with distance from the leading edge. The Reynolds number at the plate trailing edge was approximately 180 million. Note that the plot is a log-log type with the symbols indicating the stream-wise distribution of the grid points. The high Reynolds number was obtained through increasing the free-stream total pressure, rather than physically lengthening the flat plate geometry. The normalized velocity and shear stress distributions at $R_\theta = 1420$ and 100,000 are shown in figures 3 and 4. The comparisons at $R_\theta = 1420$ are compared with the DNS calculations of Spalart, ref. 15, and at $R_\theta = 100,000$ are compared with the classical flat plate equations. All three ASM match fairly closely the DNS calculation shown in figure 3, with the Girimaji model following the closest in the buffer region. All three models were slightly above the DNS at the edge of the boundary layer. Similarly, Girimaji best fit the DNS stress profile, $u'v'^{+} = (\partial u/\partial z)C_\mu f_\mu K^2/\varepsilon/u_\tau$, though all three ASM were generally a good match. The high Reynolds number comparisons, figure 4, at $R_\theta = 100,000$, approximately $N_{R_\theta} = 90$ million, have trends fairly consistent with the classical flat plate boundary layer flow equations. The stress profiles, figure 4(b), have similar lower level behavior (below $y^+ = 50$) as the lower Reynolds number profiles and a greatly flattened region of constant stress below the boundary layer edge around $y^+ = 30,000$. The grid had typically 2 cells less than $y^+ = 2.5$ and about 36 cells in the boundary layer at $R_\theta = 1420$.

Flat Plate Skin Friction Figures 5 and 6 are a comparison of classical flat plate theories for local and average skin friction with the three ASM solutions. The equations for the local skin friction comparisons were:

$$c_f = \begin{cases} 0.664/\sqrt{R_x}, & \text{Blasius ;} \\ 0.0590 {R_x}^{-\frac{1}{5}}, & \frac{1}{5}th \text{ power law;} \\ 0.455/ln^2(0.06R_x), & \text{White-"Exact" theory.} \end{cases} \tag{12}$$

The equations for the average skin friction were:

$$C_F = \begin{cases} 1.328/\sqrt{R_L}, & \text{Blasius:} \\ 0.455/(log_{10}^{2.58}(R_L) - A/R_L), & \text{Transition:} \\ 0.074 {R_L}^{-\frac{1}{5}} - A/R_L, & \frac{1}{5}th \text{ power law;} \\ 0.523/ln^2(0.06R_L). & \text{White-"Exact" theory.} \end{cases} \tag{13}$$

where $A = R_{crit}(C_{F_t} - C_{F_l})$. $C_{F_l} = 1.328/\sqrt{R_{crit}}$. $C_{F_t} = 0.074(R_{crit})^{-\frac{1}{5}}$.

R_{crit} is the local Reynolds number at the point of transition from laminar to turbulent flow. Transition was defined as the point at which the shape factor H_{12} first fell below 2.3. Local skin friction and average skin friction coefficients and normalized turbulent viscosity are plotted in figures 7, 8 and 9, respectively for all three of the algebraic Reynolds stress models. Girimaji, SZL and GS ASMs predict similar and consistent skin friction characteristics throughout the Reynolds number range. All three models were virtually identical in local and average skin friction for the laminar flow that developed upstream of the transition trip point at $R_x = 300,000$. Downstream of the trip, the Girimaji model developed slight higher local skin friction that the other two ASM, with subsequently higher average skin friction. All three models departed from the 1/5th power theory for local skin friction at Reynolds numbers above 20 million. The skin friction predicted by Girimaji's model was slightly above the higher Reynolds number theory of White, while the other two tracked slightly low.

The trend of average skin friction through transition to turbulent flow was similar between the three models and followed the 1/5th power theory very closely until, again departing around 20 to 30 million Reynolds number, figure 6. Figure 7 is a plot of the growth of turbulent viscosity normalized by the local laminar viscosity with R_{δ_1}. Girimaji's model predicts the highest level of normalized turbulent viscosity, though all three models are very similar in level and rate of growth.

Boundary Layer Shape Factors – All three ASM have very similar shape factor H_{12} trends as shown in figure 8. The first 8 or so computational cells were neither laminar nor turbulent as the solution developed. The subsequent 28 cells matched the theoretical laminar characteristics very closely. The theoretical turbulent shape factor was not closely achieved until around $R_x = 20$ million. Even though transition from laminar flow occured relatively quickly, formation of a turbulent shape factor close to the theoretical shape required some distance to achieve. All three models very closely match the turbulent shape factor of $H_{12} = 1.27$ at very high Reynolds numbers.

Overall, all three non-linear turbulence models appear to be consistent and well behaved turbulent flat plate properties up to Reynolds numbers of 180 million.

Axisymmetric Afterbody

Test Facility--The second test case was an axisymmetric geometry that was part of a series of models tested in both the Langley 1/3m Pilot Transonic Cryogenic Tunnel and the 16-Foot Transonic Tunnel. The Pilot Tunnel had an octagonal test section with slots at the corners of the octagon and is essentially a scale model of the Langley 16-Foot Transonic Tunnel test section, ref. 16. The test medium for the cryogenic tunnel was nitrogen cooled by liquid nitrogen. High Reynolds number data were obtained in the 0.3m tunnel through a combination of cryogenic free-stream temperatures and free-stream total pressure that are independently controllable. Approximately 5 atm. of pressure and 100K total temperature produced a unit Reynolds number of 260 million/meter.

The experiment was conducted over a range of temperatures from approximately 100K to 300K and pressures from 1 to 5 times the standard atmospheric level. Several settings of free-stream total temperatures or pressures can result in identical settings of Reynolds number. Surface pressure coefficients and nozzle boattail drag were shown to be similar regardless of the temperature/pressure combinations that created equivalent Reynolds numbers, ref. 2. High Reynolds number simulations with the CFD method were obtained through increased total pressure rather than through a combination of free-stream total pressure and cryogenic temperatures. Though data were obtained over range of Mach number from 0.6 to 0.9, only the M = 0.9 data is compared with the CFD in this paper. The following is a table of conditions for experimental data obtained at M = 0.9 for the L/d_m = 16.0 model. One atmosphere is defined at 0.101325 MPa (14.703 psi).

M_∞	T_{t_0},K(R)	p_{t_0},atm	$N_{Re} \times 10^6$
.903	106 (191)	4.98	128
.908	118 (212)	3.98	87
.901	119 (214)	2.98	64
.911	118 (212)	2.47	55
.910	118 (212)	1.97	43
.904	119 (214)	1.49	32
.903	118 (212)	1.24	27
.899	312 (562)	4.97	28
.899	308 (554)	3.79	22
.902	308 (554)	2.48	14
.901	307 (553)	1.23	7

Geometry--The configuration used for this study was one of six models that were built for the original Reynolds number study, ref. 1. Four models with differing boattail geometry were associated with a body length of 8 inches from the nose to the start of the boattail (characteristic length) and two models with a characteristic length of 16 inches. The boattail geometries had circular arc, circular arc-conic, or contoured profiles. This investigation utilized the circular arc with a length-to-maximum-diameter ratio (fineness ratio) of 0.8 boattail. Figure 9 is a photograph of the model mounted in the pilot tunnel. The nose of the model was a 28° cone 1.7956 inches long fairing to the cylindrical body via a 1.3615 inch radius circular arc whose center is 2.125 downstream of the model nose and 0.8615 inches below the model centerline. The circular arc fairing is tangent at its endpoints to the conical nose (1.7956 inches from the nose) and cylindrical body (2.125 inches from the nose). The model was sting mounted with the diameter of the sting being equal to the model base diameter. The length of the constant diameter portion of the sting (6.70 inches measured from the nozzle connect station) was such that, based on the work of Cahn, ref. 17, there should be no effect of the sting flare downstream of the nozzle trailing edge on the boattail pressure distributions.

The axisymmetric afterbody grid utilized H-O type mesh topology with all block dimensions that were divisible by 4. The mesh was gridded with a single cell 5 degree wide wedge grid with the stream-wise flow direction oriented along the j index to utilize the implicit flow solver in the code for faster solution convergence. The body was described using 100 cells extending from the leading edge of the nose to the nozzle connect station. There were 80 cells extending from the nozzle connect station to the nozzle boattail trailing edge.

The free-stream conditions for axisymmetric CFD cases were M = 0.9, $T_{t_0} = 540R$ using air at $\gamma = 1.4$. The first cell height of each configuration's grid was different for each free-stream Reynolds number according to the following schedule.

Reynolds number	p_{t0},atm. (psi.)	h_1 (inches)
7	1.2 (17.8)	6×10^{-5}
55.2	9.52 (140.)	8×10^{-6}
128.3	22.1 (325.)	2×10^{-6}

The wind tunnel models were constructed of cast aluminum with stainless-steel pressure tubes cast as an integral part of the model. The model was instrumented with 30 pressure orifices in three rows of 10 orifices each. The 1 inch diameter of the model physically precluded the placement of all 30 orifices along the same row. The following is a tabulation of the non-dimensional orifice locations.

x/d_m for L/d_m = 16 at		
$\phi = 0°$	$\phi = 120°$	$\phi = 240°$
-0.4491	-0.4660	-0.4561
-.1637	-.2201	-.1552
-.0600	-.1281	-.0590
.0337	-.0260	.0390
.1268	.0744	.1342
.2279	.1729	.2713
.3210	.2696	.3718
.4199	.3679	.4680
.5231	.4640	.5749
.6279	.6758	.7304

Grid convergence--Figures 10 and 11 show grid sensitivity of the Girimaji ASM at M = 0.9 at the lowest and highest Reynolds number for this test case, N_{Re} = 7 and 128 million, respectively. These sensitivities were relatively consistent for the other turbulence models and other viscous models investigated. A few exceptions occurred where the coarse grid solution did not converge, but the following medium and fine grid solutions converged and the results were similar in nature as those shown in figures 10 and 11. All solutions were fairly well grid converged and solution converged. Initial inspection of figure 11, the coarse grid solution has the closest match with the data. Further refinement of the grid revealed this solution to not be grid converged. Converged solutions for this geometry appear to require between 40

to 80 cells along the nozzle boattail to adequately predict the shock-separated flow reasonably accurately.

Low Reynolds number Computations - Figures 12 through 16 are low Reynolds number calculations showing the effect of turbulence model, turbulent trip location and viscous model on pressure coefficient and turbulent kinetic energy distributions.

In figure 12 all the calculations were performed with using a single thin-layer viscous model, i.e., k-thin layer for this mesh, the min-mod solution limiter, and a turbulent trip point, trip 1, approximately 0.031 inches (0.08 cm) downstream of the nose. The three ASM predicted a shock strength slightly weaker than the data and a pressure recovery slightly lower than the data. The Standard $K-\varepsilon$ model, in this instance, appears to have better agreement with the data closely matching peak negative pressure and recovered to a static pressure only slightly above that of the data at the boattail trailing edge. Figure 13 is a plot of the peak turbulent kinetic energy for each turbulence model using the same parameters as the calculations in figure 12. For clarity, two areas of the axisymmetric body are detailed, the region downstream of the nose where the turbulent trip occurs and the region around nozzle boattail. The large spike in K/a^2 just downstream of $x/d_m = -16.$ is the turbulent trip impulse in k. None of the four turbulent models tested developed turbulent flow immediately downstream of the trip. The Standard $K-\varepsilon$ linear model developed turbulence first as seen by the rise in K/a^2 around $x/d_m = -15.7$. The Girimaji and SZL ASM became turbulent around $x/d_m = -15.3$, and GS became turbulent the furthest downstream at $x/d_m = -14.4$.

Early studies simulating the incompressible flat plate flow displayed similar characteristics. If the turbulent trip was placed upstream of the critical flow point, turbulence would not develop immediately downstream of the trip. Conversely, turbulence would develop immediately when the turbulent trip was placed downstream of the critical flow point. Considering this, a different turbulent trip point was chosen roughly between the furthest upstream and downstream turbulent development points noted previously and solutions re-developed for the three ASM. Figures 14(a) through (c) show that downstream of the cone-cylinder transition of body shape, approx. $x/d_m = -13$, despite the different initial development of turbulence, (trip 1 upstream trip@ $x/d_m = -15.969$ versus trip 2 downstream trip@ $x/d_m = -15.000$) no significant changes occur in the peak turbulent kinetic energy. Figure 15 is representative of the lack of influence on static pressure coefficient distribution on the nozzle boattail between the two turbulent trip points using the min-mod solution limiter. Further parametric studies are needed to determine the boundary layer behavior using other solution limiters with changes in the laminar-to-turbulent flow regions.

Figure 16 is a study of the effect of different viscous models on the flow on the afterbody. Three calculations were performed using k-thin layer (321): j-k viscosity coupled (322): and j-k viscosity uncoupled (323) viscosity models with Girimaji ASM at 7 million Reynolds number. The use of j-k viscosity appears to improve the comparison with experimental data by creating a shock slightly stronger and further downstream than the k-thin layer calculation, in addition to slightly raising the pressure recovery in the region of separated flow. As will be shown subsequently, the observations of best comparison with data will change with Reynolds number.

High Reynolds number Computations - Figures 17 through 21 are high Reynolds number calculations showing the effect of turbulence model and viscous model on pressure coefficient and turbulent kinetic energy distributions on the body. Figure 17 is a comparison of the four turbulence models at $N_{Re} = 128$ million using k-thin layer viscosity, min-mod limiter and trip1 for turbulent tripping. The three ASM cluster around the experimental data matching the pressure recovery in the separated flow region considerably better than at low Reynolds numbers. The Standard $K-\varepsilon$ model predicts the strongest shock and highest pressure recovery.

Figure 18 is the plot of peak turbulent kinetic energy similar to figure 13 for the four turbulence models. Significantly, all four models developed turbulent flow immediately downstream of the turbulent trip as seen by the four curves departing from the trip spike in K/a^2 at levels around 0.004. Each turbulence model remained at slightly different levels, but had similar trends until the region of flow involving the shock-separation downstream of $x/d_m = 0.25$. The trend of the peak turbulent kinetic energy was similar to the 7 million Reynolds number trend in figure 13. Though the three ASM have very similar static pressure coefficient distributions, figure 17, the peak K/a^2 trends are completely different. Also, the C_p distributions between SZL and the Standard $K-\varepsilon$ model are very different, but the peak K/a^2 have similar trends and levels. Therefore at this point, a correlation between the trend of K/a^2 and C_p can not be made.

Figure 19 is the effect of viscous model using the Girimaji ASM at 128 million Reynolds number. In this instance, the k-thin layer calculation (321) provides the best comparison with the experimental pressure coefficient distribution. The j-k viscous models behaved similarly in that the shock strength increased and the recovery pressure was higher than the k-thin layer calculation. Figure 20 is the peak K/a^2 for the three viscous models shown in figure 19. The three viscous models have similar trends in peak turbulent kinetic energy until the region of shock-separated flow downstream of $x/d_m = 0.25$. Both j-k viscous models generate higher peak turbulence than the k-thin layer model. The plots in figures 21(a) to (c) are contours of turbulent kinetic energy predicted by the three viscous models previously discussed. The k-thin layer viscous model, figure 21(a), has an abrupt discontinuity in the flow-field around the boattail trailing edge, $x/d_m = .8$, while the both j-k viscous models predict very smooth and continuous contours from the region of the shock, $x/d_m = .25$, to downstream.

Reynolds number Trends - Figures 22 through 27 are trends of integrated boattail pressure drag, skin friction, and predicted point of flow separation with Reynolds number. The integrated pressure drag variation with Reynolds number comparing CFD with experiment is shown in figure 22. Despite the changes in the shock strength and pressures on the nozzle boattail with Reynolds number: the variation in pressure drag was small. Overall, the predicted level of pressure drag was slightly below that of the experimental data, though at the low and high Reynolds numbers the CFD was almost within the scatter of the experimental data. As a point of reference, 3 additional data points are plotted to

include data obtained for the short cryogenic models tested in the 16 Foot Transonic Tunnel at Langley, and the original 48 inch model also test in the 16 Foot Tunnel.

Figure 23 shows the predicted change in static pressure coefficient distribution with Reynolds number. The largest change seems to occur from the very low Reynolds number to the mid-range, with the code predicting a large increase in the peak velocity, a downstream shift of the peak and a slight elevation of the static pressure of the flow in the region of separation. Considerably less change was predicted between the mid-range Reynolds number to the high Reynolds number of 128 million.

Figure 24 is a bar chart of the integrated pressure drag on the boattail at 7 million Reynolds number comparing the different viscous models and trip location predicted drag with the Girimaji ASM with experimental data. The higher recovery pressure that occurred through the j-k viscosity calculations reduced the integrated pressure drag from 37 to roughly 28 nozzle drag counts. The scatter in the CFD results is about the same as the experimental results with the exception of the 48 inch model data tested in 16-Foot.

High Reynolds number comparisons are shown in Figure 25 with the addition of GS, SZL and Standard $K-\varepsilon$. The scatter in the CFD is similar to the low Reynolds number comparison with the Standard $K-\varepsilon$ predicting the lowest drag due to the considerably higher pressure recovery at the boattail. Girimaji and SZL, k-thin layer, are the closest to the experimental data, though on the average are low.

Variation of predicted skin friction coefficients for Girimaji ASM with Reynolds number is plotted against flat plate wetted area estimations in figure 26. In general, the CFD predicts skin friction coefficients are 3.5 nozzle drag counts low at 7 million Reynolds number and about 1.5 nozzle drag counts low at 128 million Reynolds number. Considering the flow effects not accounted for by the flat plate wetted area calculations, (e.g., non-constant Mach number, adverse/favorable pressure gradients, aft-projected areas and separated flow) this comparison is fairly good.

Lastly, figure 27 is an analysis of the predicted point of flow separation with Reynolds number comparing with some flow visualization data obtained in the 16 Foot Transonic Tunnel on the 48 inch model in 1974 and the parametric theory of Reshotko-Tucker, ref. 18. The separation observed in ref. 18 was somewhat three dimensional with the estimated extent thereof shown by the spread in open triangles in the figure. No separation data are available for this model at any of the other Reynolds numbers. The SZL ASM predicted a flow separation point that more closely matched the wind tunnel measurement and Reshotko-Tucker predictions with increasing Reynolds number. Both Girimaji and GS predicted flow separation points further downstream. The j-k viscosity predictions of Girimaji predicted the least separated flows, with the j-k coupled viscosity calculation predicting practically no separated flow at 7 million Reynolds number.

Remarks

1. The high Reynolds number boundary layer calculation of skin friction and shape factor for the subsonic flat plate was consistent with theoretically predicted behavior.
2. The linear turbulence simulation predicted a shock further downstream and a recovery pressure higher than the non-linear turbulence simulations at the low and high Reynolds numbers.
3. The best performance combination of turbulence models and viscous models appears to change from low Reynolds number to very high Reynolds number. The ASM with j-k viscous modeling appeared to provide the best low Reynolds number comparison, while ASM with only k-thin layer viscosity most closely matched the high Reynolds number static pressure coefficient distribution. Further investigation is required to resolve this issue.
4. The afterbody pressure drag variation observed in the experimental data and the computations with Reynolds number was small. The change with Reynolds number of the pressure coefficient distribution observed in the experimental data is qualitatively predicted by the CFD. This "no-effect effect" had been discussed in the previous high Reynolds numbers investigations.
5. Most of the solutions using the non-linear models predicted a separation point downstream of experimental flow visualization and parametric theory except the model by Shih, Zhu and Lumley.

References

1. Reubush, D. E.; and Putnam, L. E.: An Experimental and Analytical Investigation of the Effect on Isolated Boattail Drag of Varying Reynolds Number up to 130×10^6. NASA TND-8210, May 1976.
2. Reubush, D. E.: The Effect of Reynolds number on Boattail Drag. AIAA-75-63, AIAA 13th Aerospace Sciences Meeting, January 20–22, 1975.
3. Reubush, D. E.: The Effect of Reynolds number on Boattail Drag of Two Wing-Body Configurations. AIAA-75-1294, AIAA/SAE 11th Joint Propulsion Conference, September 29–October 1,1975.
4. Reubush, D. E.: Experimental Investigation to Validate Use of Cryogenic Temperatures to Achieve High Reynolds Numbers in Boattail Pressure Testing. NASA TM X-3396, August, 1976.
5. Abdol-Hamid, K. S.; Carlson, J. R.; and Lakshmanan, B.: Application of Navier-Stokes Code PAB3D to Attached and Separated Flows for Use With $K-\epsilon$ Turbulence Model. NASA TP-3480, 1994.
6. Abdol-Hamid, K. S.: A Multiblock/Multizone Code (PAB3D-v2) for the Three-Dimensional Navier-Stokes Equations: Preliminary Applications. NASA CR-182032, October 1990.
7. Abdol-Hamid, K. S.; Carlson, J. R.; and Pao, S. P.: Calculation of Turbulent Flows Using Mesh Sequencing and Conservative Patch Algorithm. AIAA 95-2336, 31st. Joint Propulsion Conference, July 1995.
8. Abdol-Hamid, K. S.: Implementation of Algebraic Stress Model in a General 3-D Navier-Stokes Method (PAB3D). NASA CR-4702, December 1995.
9. Krist, S. L.; Thomas, J. L.; Sellers, W. L; and Kjelgaard, S. O.: An Embedded Grid Formulation Applied to a Delta Wing. AIAA 90-0429, 28th Aerospace Sciences Meeting, Jan. 8-11, 1990.

10. Patel, V. C.; Rodi, W.; and Scheuerer G.: Turbulence Models for Near-Wall and Low Reynolds Number Flows: A Review. AIAA Journal, Vol. 23, No. 9, pp. 1308-1319, September 1985.

11. Launder, B. E. and Sharma, B. I.: Application of the Energy Dissipation Model of Turbulence to the Calculation of Flow Near a Spinning Disk. Letters in Heat and Mass Transfer, Vol. 1, 1974, pp. 131-138.

12. Shih, T-H; Zhu, J.; and Lumley, J. L.: A New Reynolds Stress Algebraic Model. NASA TM-166644, ICOMP 94-8, 1994.

13. Gatski, T. B. and Speziale, C. G.: On Explicit Algebraic Stress Models for Complex Turbulent Flows. NASA CR-189725, ICASE Report No. 92-58, November 1992.

14. Girimaji, S. S.: Fully-explicit and Self-consistent algebraic Reynolds Stress Model. ICASE Report 95-82, 1995.

15. Spalart, P. R.: Direct Simulations of Turbulent Boundary Layers up to $Re_\theta = 1420$. Journal of Fluid Mechanics, Vol. 187, pp. 61-98, 1988.

16. Kilgore, R. A.: Adcock, J. B.: and Edward, J.: Flight Simulation Characteristics of the Langley High Reynolds Number Cryogenic Transonic Tunnel. AIAA 74-80, Jan. 1974.

17. Cahn, M. S.: An Experimental Investigation of Sting-Support Effects on Drag and a Comparison With Jet Effects at Transonic Speeds. NACA Report 1353, 1958.

18. Abeyounis, W. K.: Boundary-Layer Separation on Isolated Boattail Nozzles. NASA TP-1226, August 1978.

Appendix

The functions and variables used in the Girimaji algebraic Reynolds stress model are listed:

$$L_1^0 = \frac{C_1^0}{2} - 1; L_1^1 = C_1^1 + 2$$

$$L_2 = \frac{C_2}{2} - \frac{2}{3}; \quad L_3 = \frac{C_2}{2} - 1; \quad L_4 = \frac{C_4}{2} - 1.$$

$$\eta_1 = \left(\frac{K}{\epsilon}\right)^2 S_{mn}S_{mn}; \eta_2 = \left(\frac{K}{\epsilon}\right)^2 W_{mn}W_{mn}$$

$$p = -\frac{2L_1^0}{\eta_1 L_1^1}; \quad r = -\frac{L_1^0 L_2}{\left(\eta_1 L_1^1\right)^2}$$

$$q = \frac{1}{(\eta_1 L_1^1)^2}\left[\left(L_1^0\right)^2 + \eta_1 L_1^1 L_2 - \frac{2}{3}\eta_1 (L_3)^2 + 2\eta_2 (L_4)^2\right]$$

$$a = \left(q - \frac{p^2}{3}\right); b = \frac{1}{27}\left(2p^3 - 9pq + 27r\right)$$

$$D = \frac{b^2}{4} + \frac{a^3}{27}; cos(\theta) = \frac{-b/2}{\sqrt{-a^3/27}}$$

The coefficients G_2 and G_3 are:

$$G_2 = \frac{-L_4 G_1}{L_0^1 - \eta_1 L_1^1 G_1}; \quad G_3 = \frac{2L_3 G_1}{L_0^1 - \eta_1 L_1^1 G_1}$$

additionally

$C_1^0 = 3.4$; $C_1^1 = 1.8$; $C_2 = 0.36$; $C_3 = 1.25$, $C_4 = 0.4$.

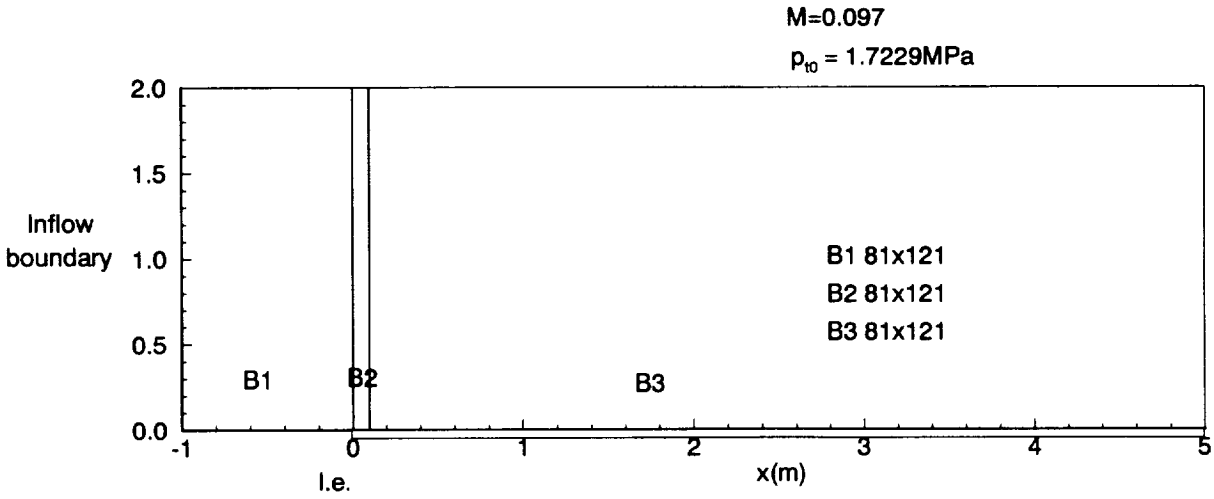

Figure 1.-Block and grid arrangement for subsonic flat plate.

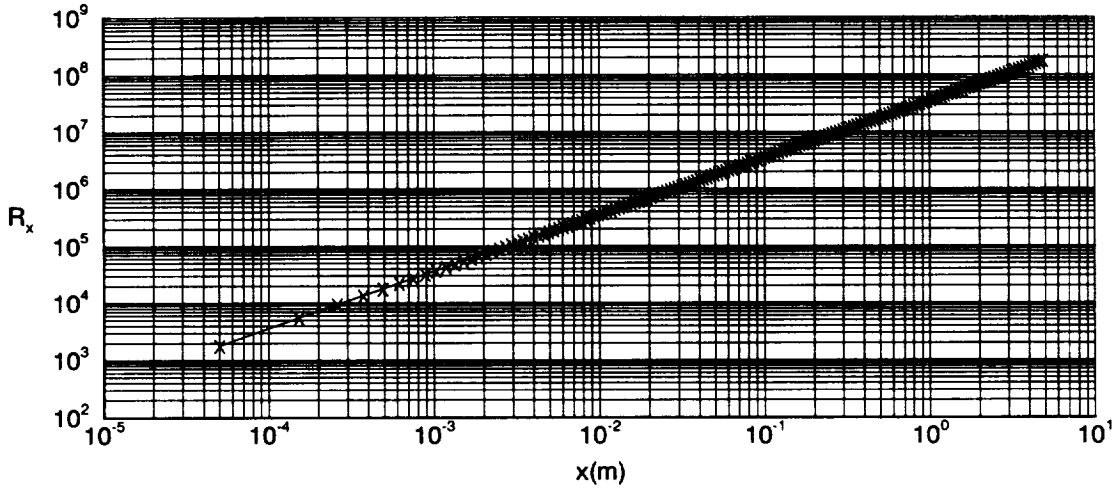

Figure 2.-Reynolds number with distance along flat plate.

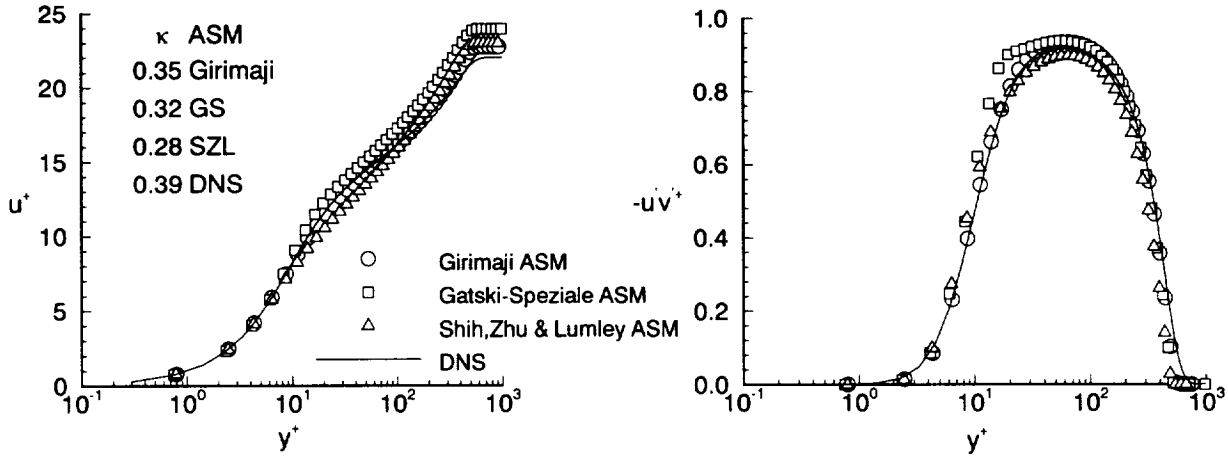

(a) Law-of-the-wall profile at R_θ=1420.

(b) Turbulent shear stress at R_θ=1420.

Figure 3.- Comparison of boundary layer characteristics for different turbulence models.

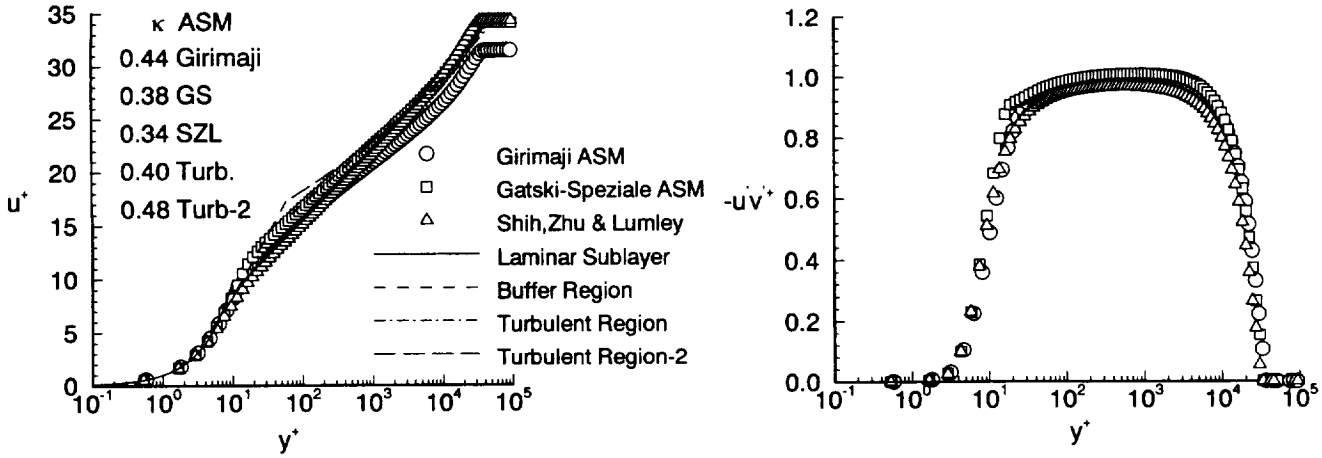

(a) Law-of-the-wall profile at R_θ=100,000.

(b) Turbulent shear stress at R_θ=100,000.

Figure 4.- Comparison of boundary layer characteristics for different turbulence models.

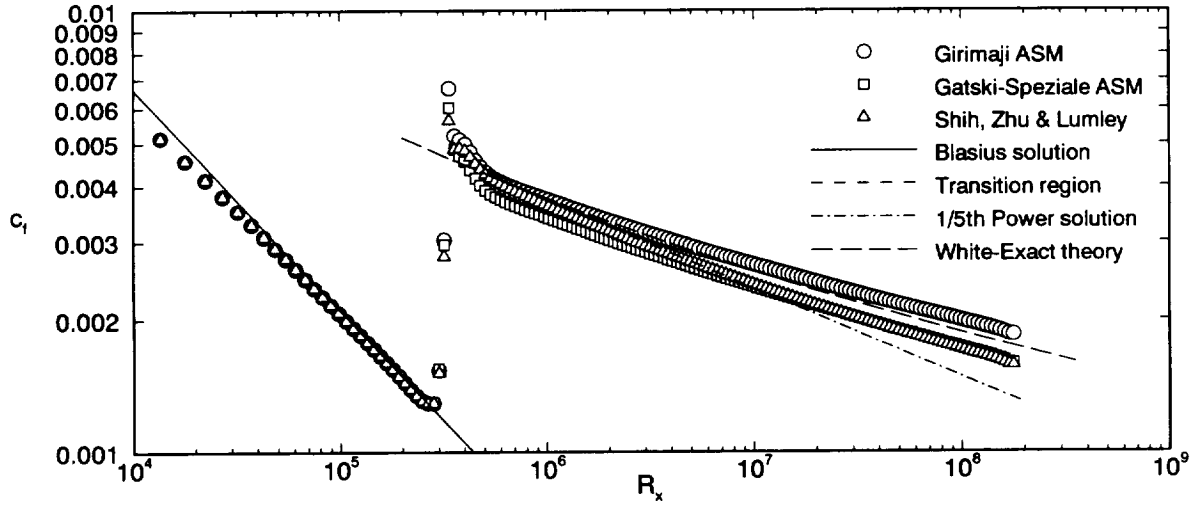

Figure 5.-Local skin friction for subsonic flat plate.

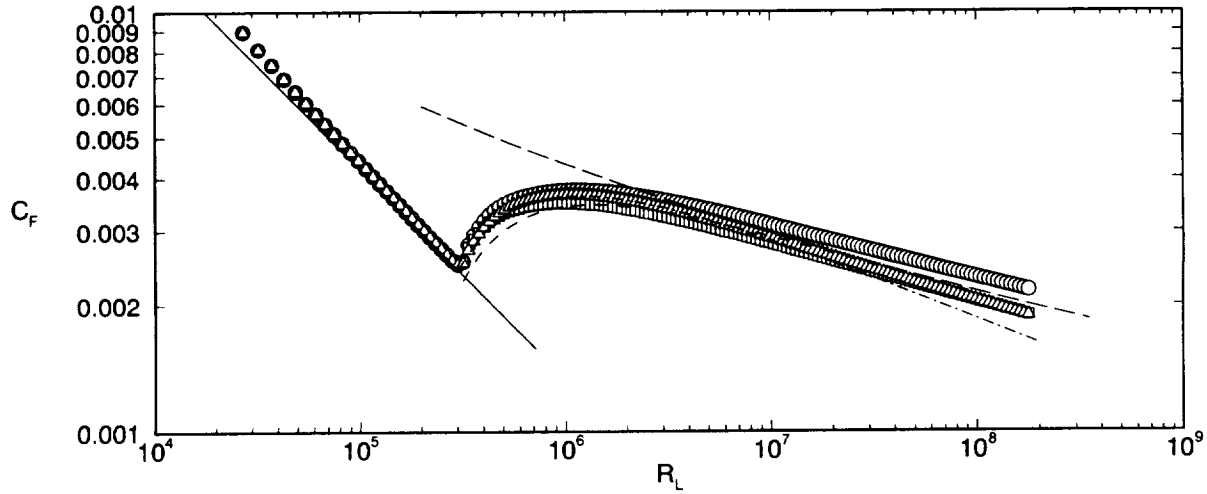

Figure 6.-Average skin friction for subsonic flat plate, (same symbol table as figure 5).

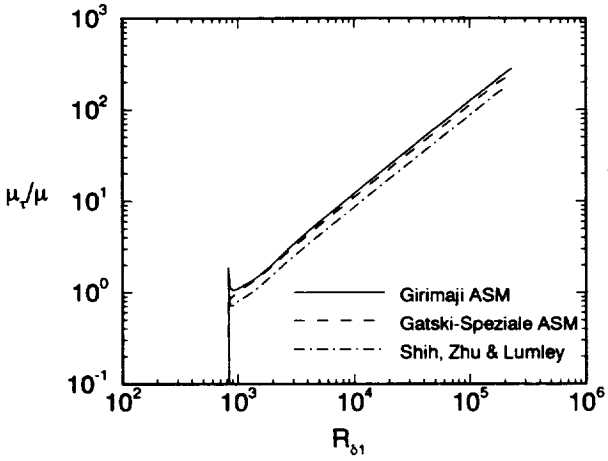

Figure 7.- Turbulent viscosity development with $R_{\delta 1}$

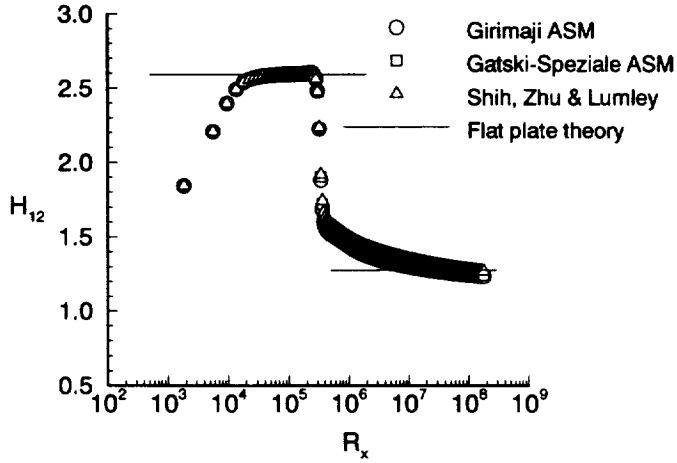

Figure 8.- Boundary layer shape factor development with R_x

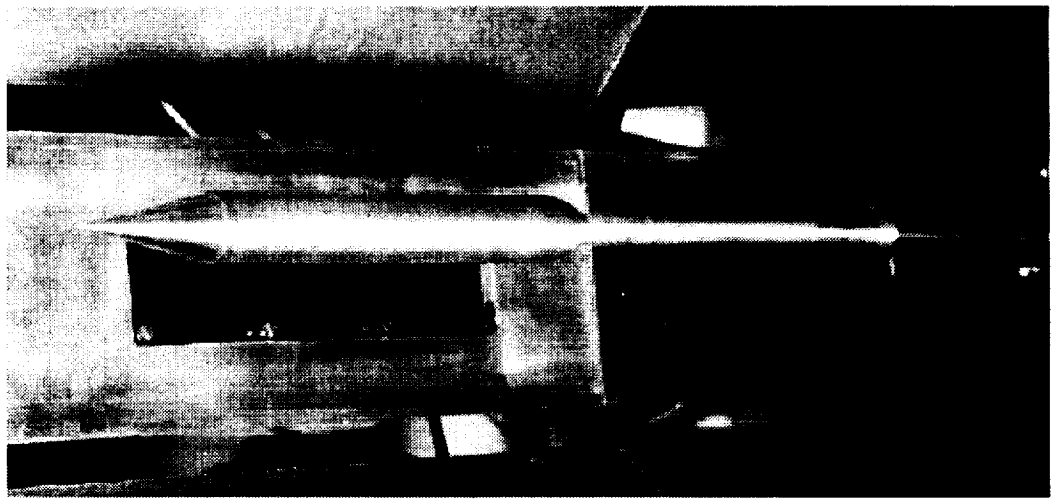

Figure 9.- Photograph of 8 inch model in 0.3m Transonic Cryogenic Tunnel.

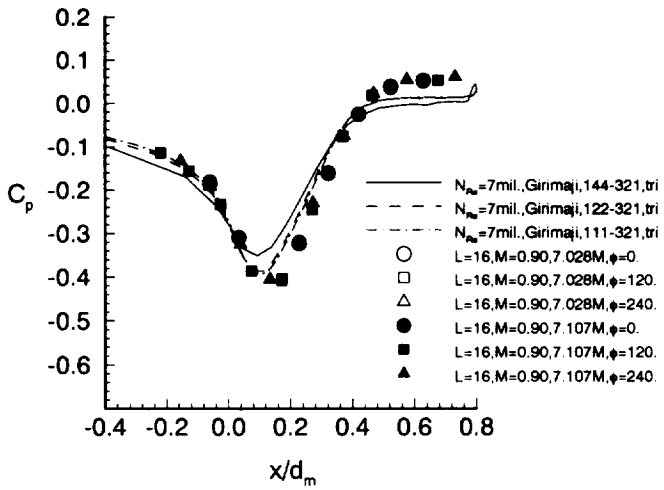

Figure 10.- Representative grid sensitivity at 7 million Reynolds number.

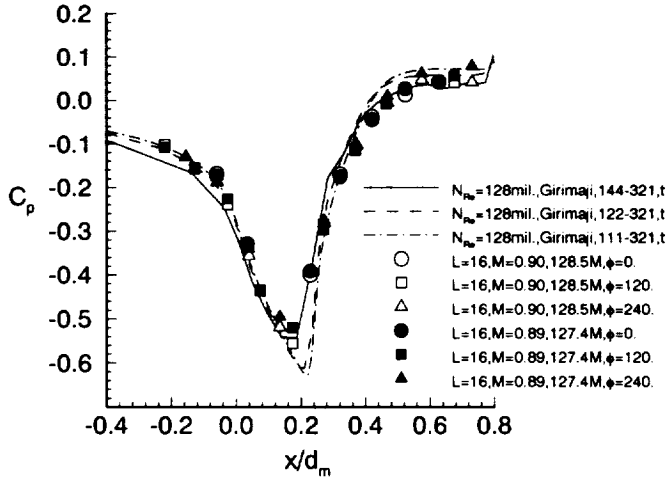

Figure 11.- Representative grid sensitivity at 128 million Reynolds number.

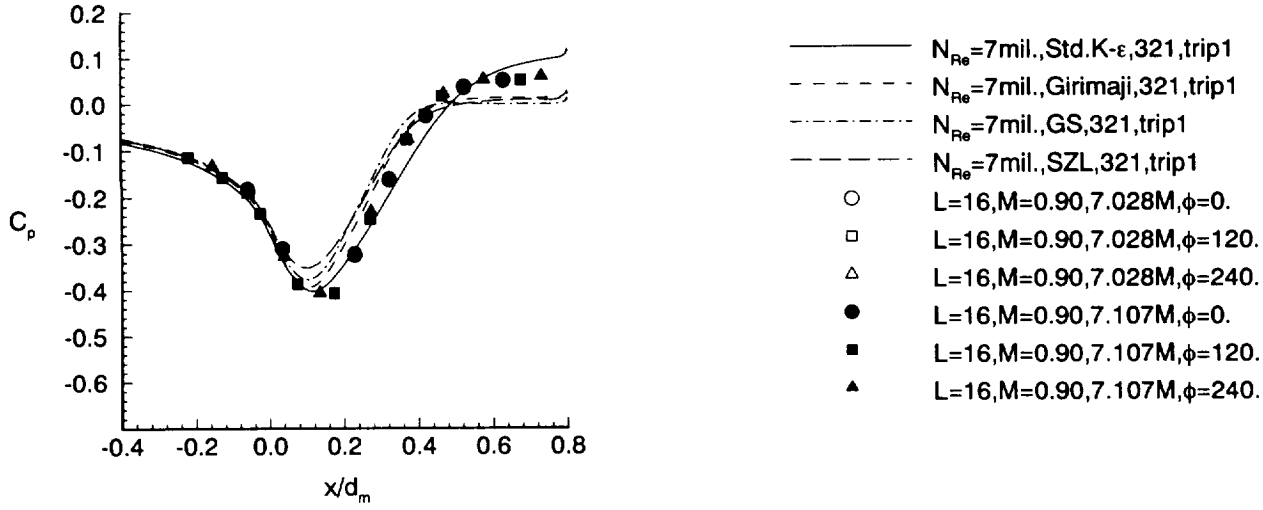

Figure 12.- Comparison of turbulence models with experimental data, M=0.9,N_{Re}=7million.

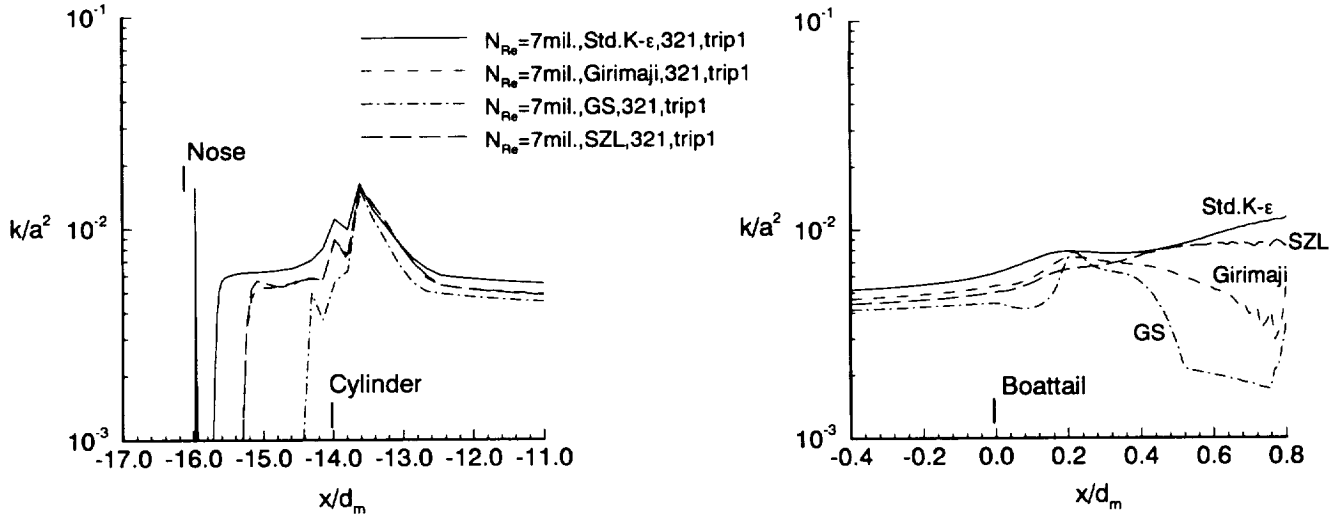

Figure 13.- Peak turbulent kinetic energy in boundary layer, N_{Re}=7million.

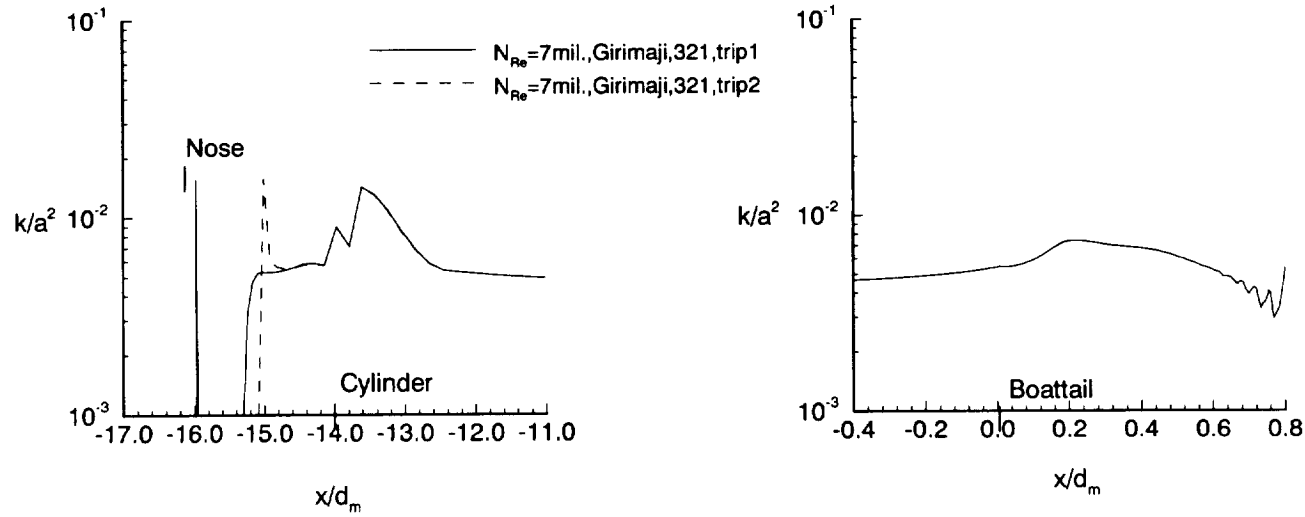

Figure 14.-Effect of trip location on turbulent kinetic energy, N_{Re}=7 million.

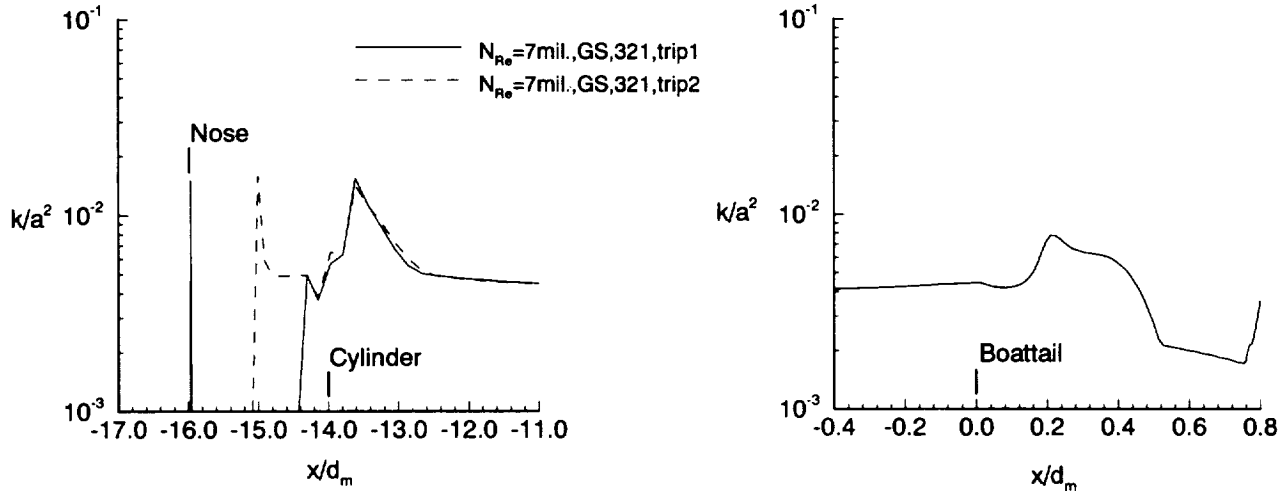

Figure 15.- Effect of trip location on turbulent kinetic energy, Gatski-Speziale, N_{Re}=7 million.

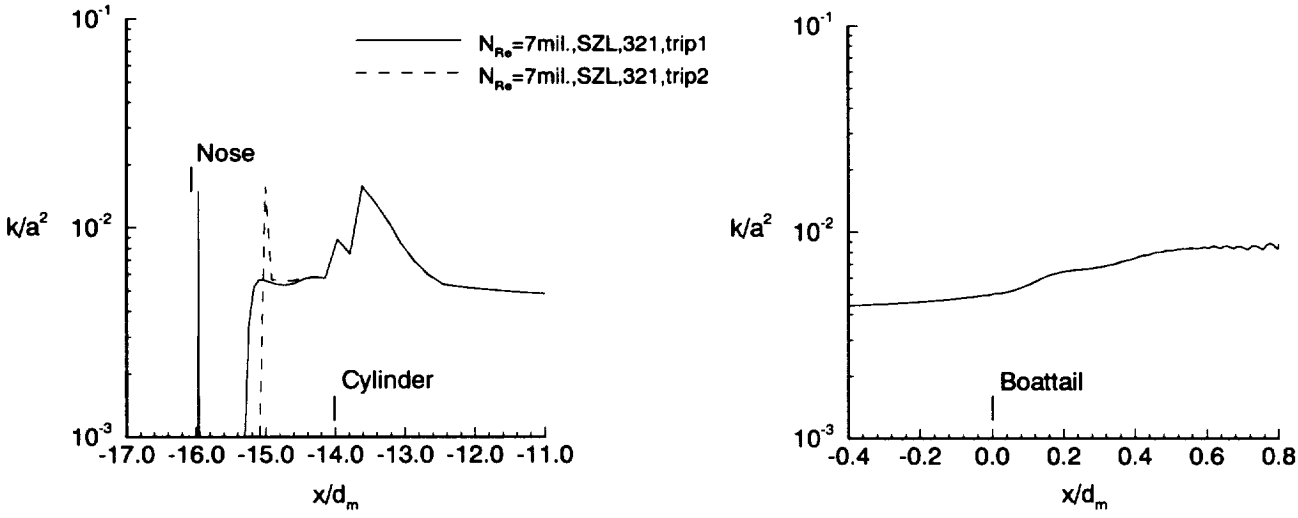

Figure 16.- Effect of trip location on turbulent kinetic energy, SZL, N_{Re}=7million.

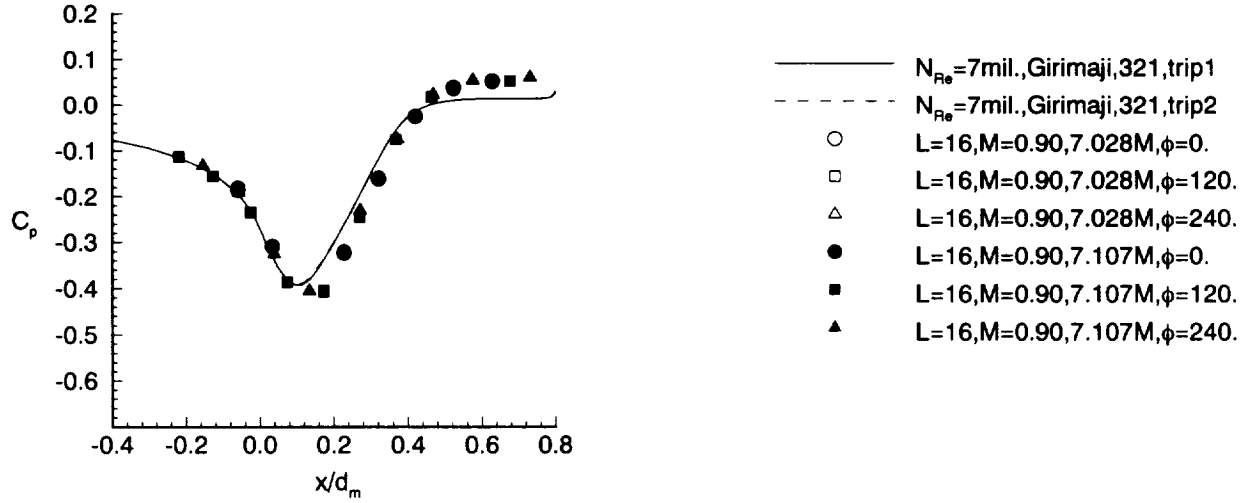

Figure 17.- Effect of trip location on nozzle pressure coefficients, M=0.9,N_{Re}=7million.

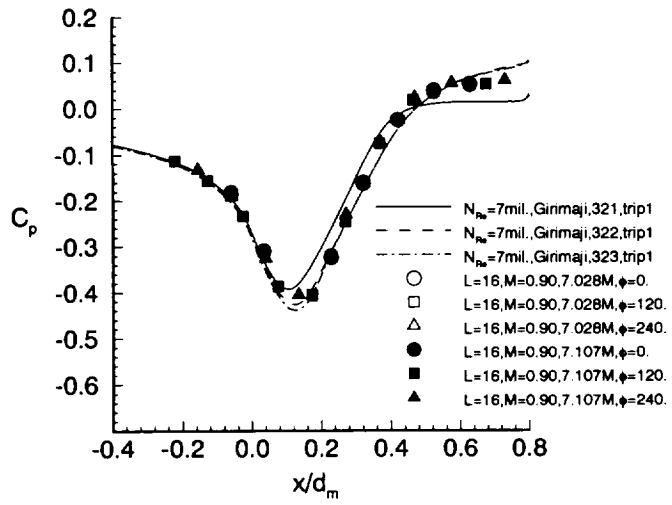

Figure 16.- Effect of viscous model on nozzle C_p distribution, N_{Re} = 7 million.

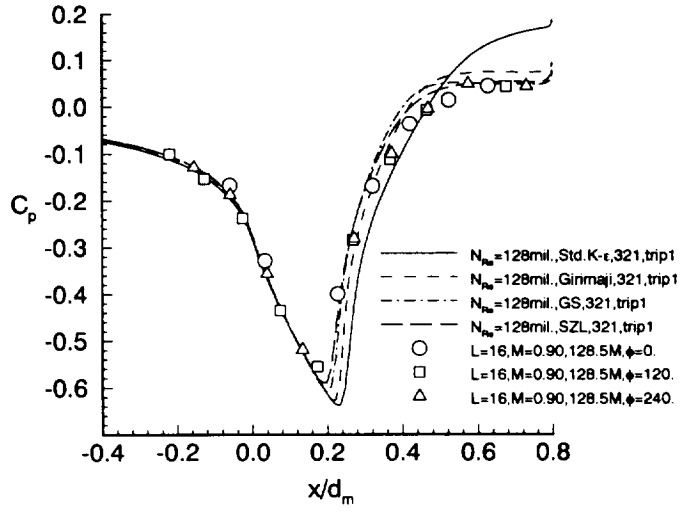

Figure 17.- Comparison of turbulence models with data, N_{Re}=128 million.

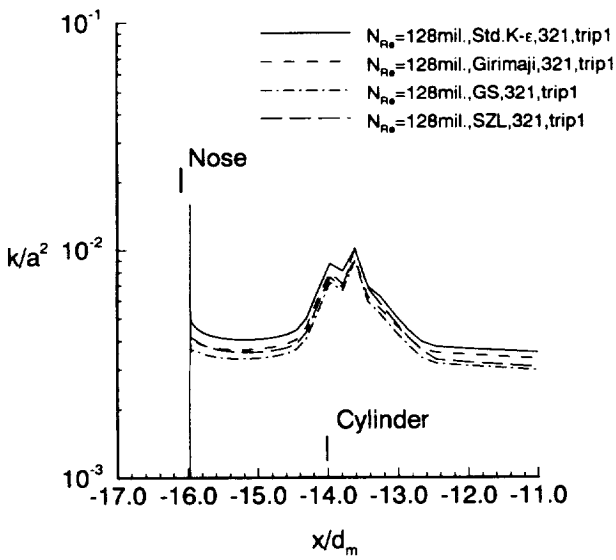

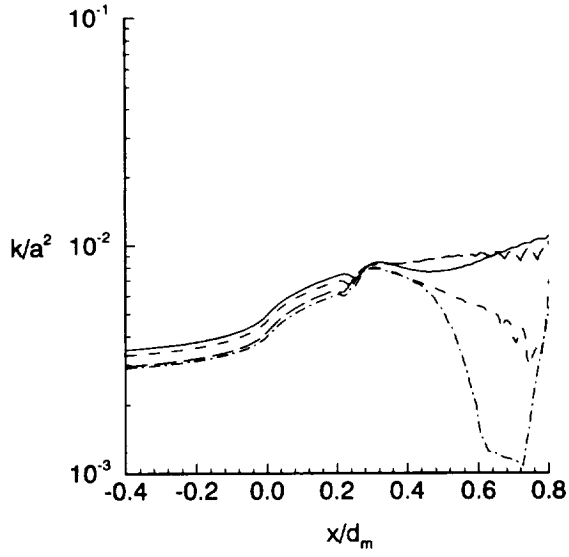

Figure 18.- Peak turbulent kinetic energy in boundary layer, M=0.9, N_{Re}=128 million.

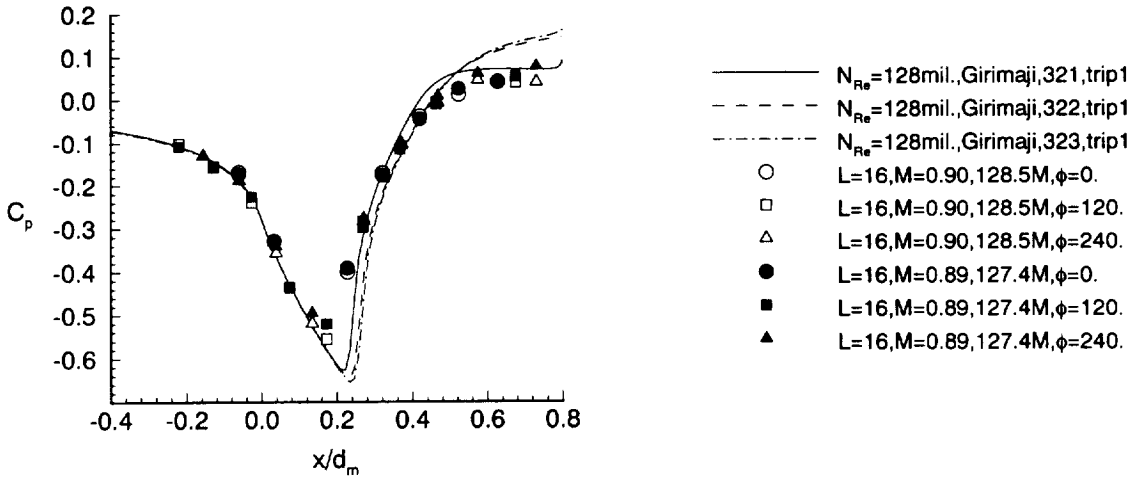

Figure 19.- Effect of viscous model on nozzle C_p distribution, N_{Re}=128 million.

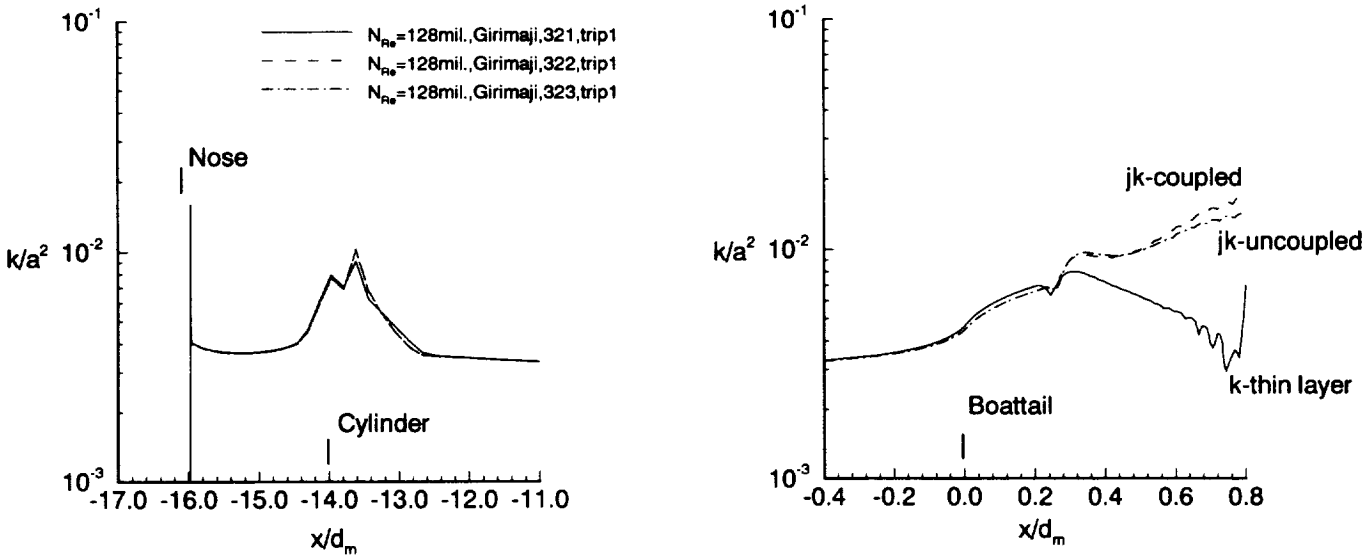

Figure 20.- Effect of viscous model on peak turbulent kinetic engery, M=0.9, N_{Re}=128 million.

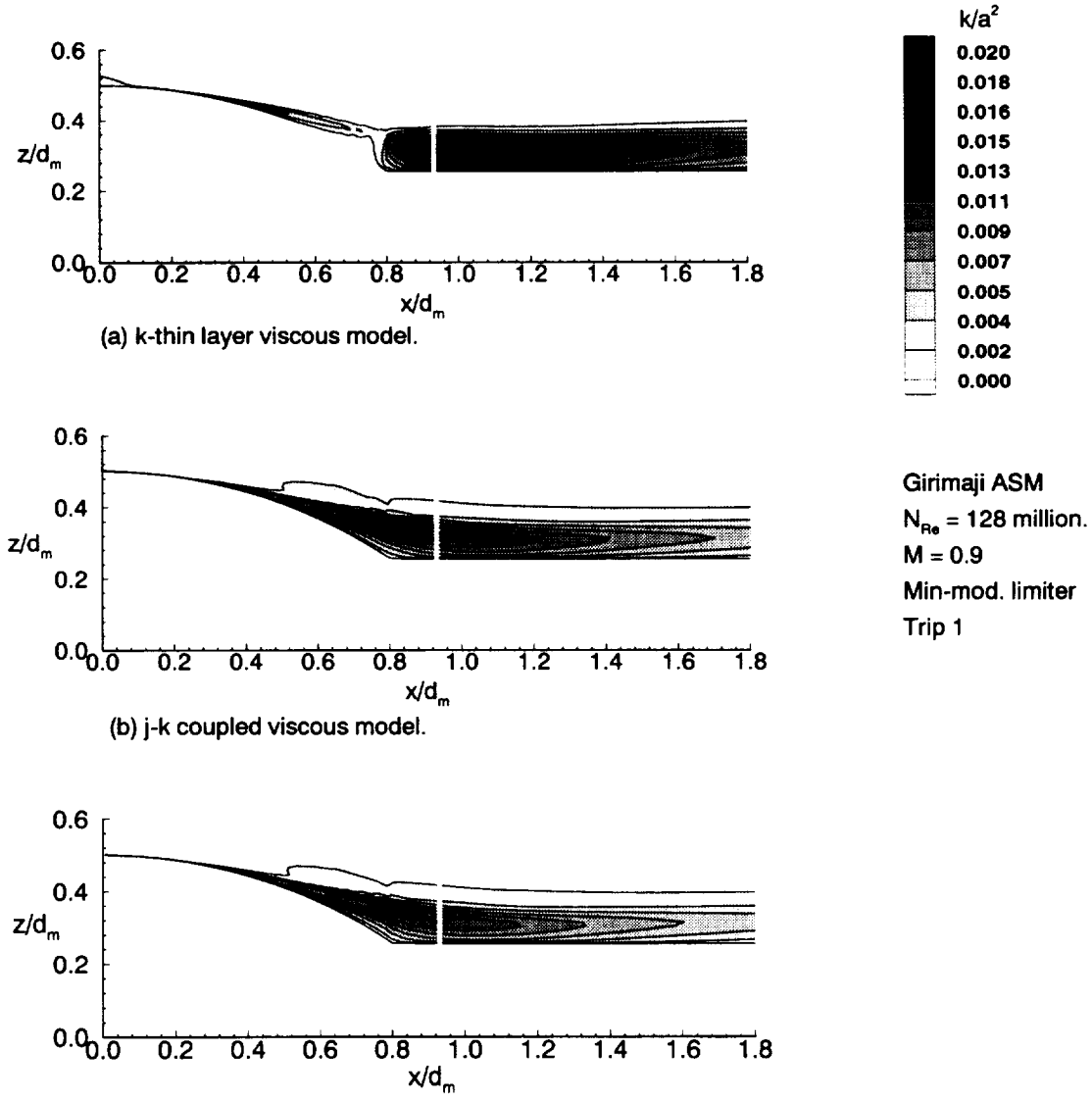

(a) k-thin layer viscous model.

(b) j-k coupled viscous model.

(c) j-k uncoupled viscous model.

Figure 21.- Effect of viscous model on turbulent kinetic energy contours.

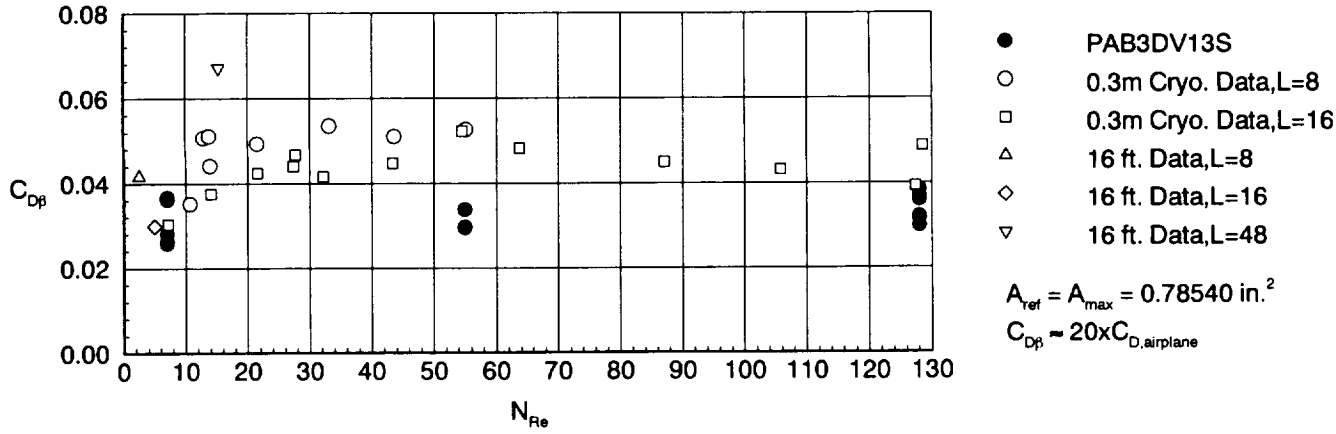

Figure 22.- Comparison of predicted integrated pressure boattail drag with experiment, M=0.9.

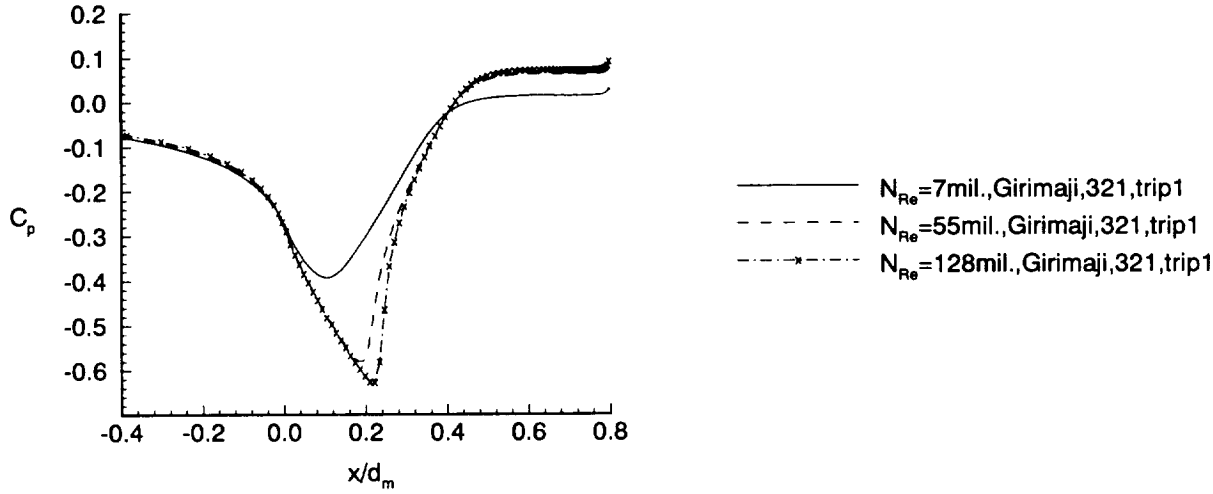

Figure 23.- Predicted variation of afterbody C_p distribution with Reynolds number, M = 0.9.

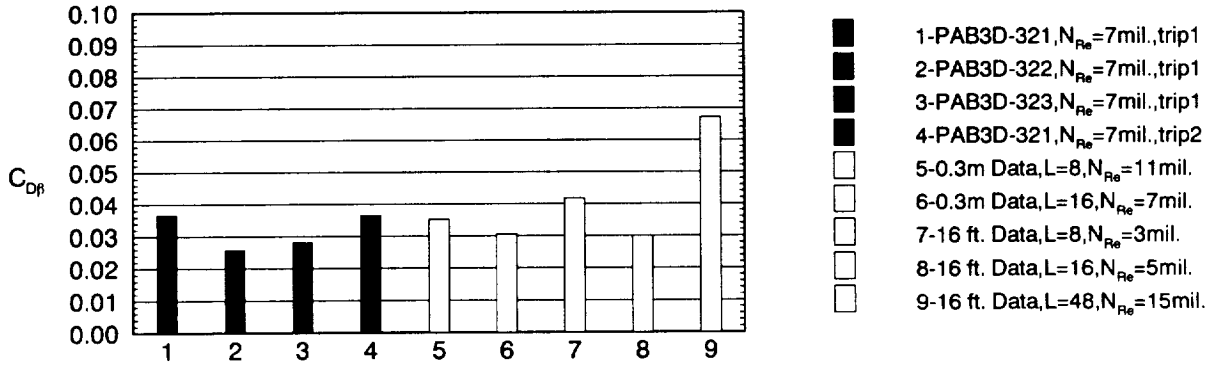

Figure 24.- Comparison of integrated boattail pressure drag at around 7 million Reynolds number, (PAB3D results using Girimaji ASM), M =0.9.

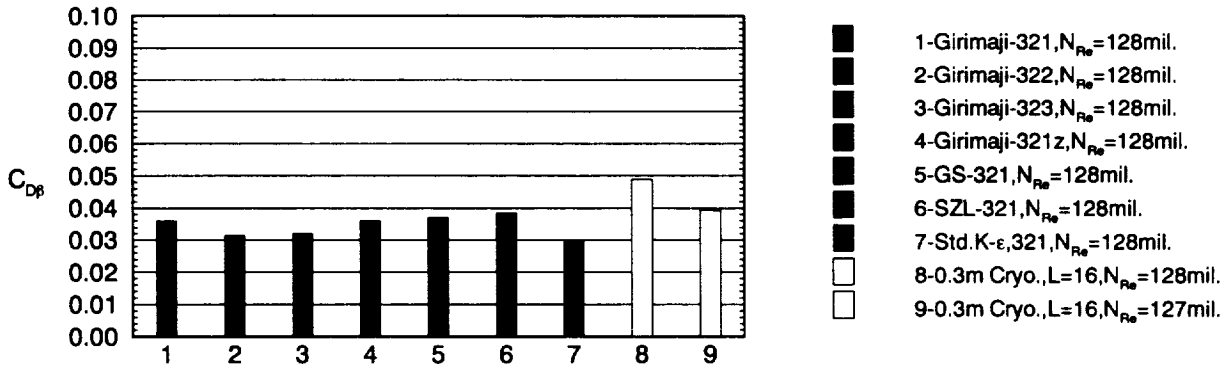

Figure 25.- Comparison of integrated boattail pressure drag near 128 million Reynolds number, M =0.9.

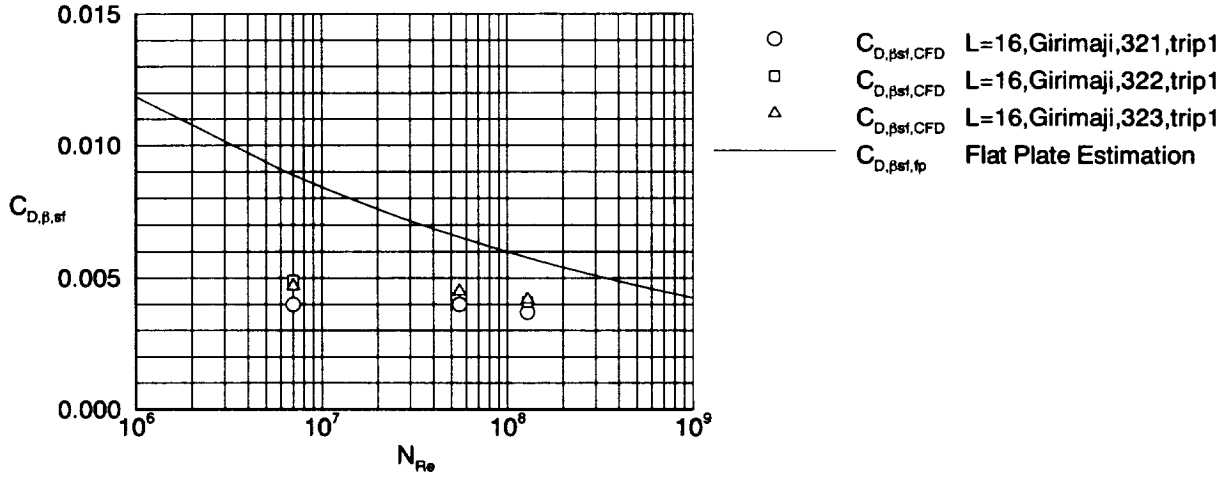

Figure 26.- Comparison of predicted skin friction coefficient with wetted-area, flat-plate estimation, M = 0.9.

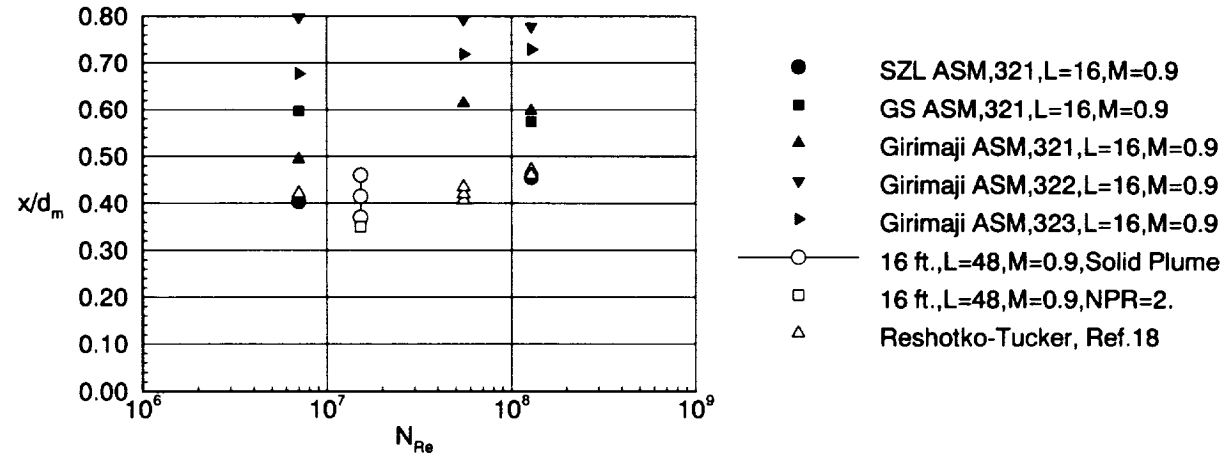

Figure 27.- Variation of predicted point of flow separation compared with flow visualized data and parametric theory.